 doi:10.20944/preprints202204.0109.v1

*Article*

# A Compact Real-time Quantitative Phase Imaging System

**Tao Peng [1,†], Zeyu Ke [1,†], Shuhe Zhang [2], Meng Shao [3], Han Yang [1,4], Xiao Liu [1], Huijuan Zou [4], Zhensheng Zhong [1], Mincheng Zhong [3], Hui Shi [1], Shu Fang [1], Rongsheng Lu [3,*] and Jinhua Zhou [1,5,*]**

[1] School of Biomedical Engineering, Anhui Medical University, Hefei 230032, China.
[2] University Eye Clinic Maastricht, Maastricht University Medical Center, P.O. Box 5800, 6202 AZ Maastricht, the Netherlands.
[3] Anhui Province Key Laboratory of Measuring Theory and Precision Instrument, School of Instrument Science and Optoelectronics Engineering, Hefei University of Technology, Hefei 230009, China.
[4] Reproductive Medicine Center, Department of Obstetrics and Gynecology, the First Affiliated Hospital of Anhui Medical University, Hefei 230032, China
[5] 3D-Printing and Tissue Engineering Center, Anhui Provincial Institute of Translational Medicine, Anhui Medical University, Hefei 230032, China.
* Correspondence: Rongsheng Lu: rslu@hfut.edu.cn; Jinhua Zhou: zhoujinhua@ahmu.edu.cn.
† These authors contributed equally to this work.

**Abstract:** Quantitative differential phase contrast (qDPC) imaging has become an important method of optical measurement and life science research in microscopy because of its high reconstruction resolution and non-invasive, high-contrast and quantitative imaging of biological samples. Despite the continuous development of the principle and algorithm, the frame rate of the existing qDPC algorithm is still much lower than that of camera acquisition, so it is hardly applied to real-time image the fast-moving biological samples. In this paper, based on color-coded multiplexing strategy, a compact real-time quantitative phase imaging system is designed to realize multi-mode imaging. The system employs a programmable LED array to illuminate directly, and the phase reconstruction algorithm is deployed in the graphics processing unit (GPU) of the laptop to accelerate the calculation. The system can achieve high-speed quantitative phase imaging of non-stained biological samples, and the frame rate can reach 60 fps. The device has the advantages of compact structure, low cost and portability. Thus, it is suitable for mobile medical applications.

**Keywords:** Self-design setup; Real-time imaging; GPU acceleration; Quantitative phase imaging; Differential phase contrast microscopy.

## 1. Introduction

Due to the fact that current optical detector can only measure the amplitude information, in biomedical applications, it is difficult to present the images of transparent samples, like unstained cells, in traditional microscopy systems as the structures of the cells are transparent to light. By staining the sample with fluorophore molecules, the cells and sub-cellular structure can be observed with high contrast[1]. However, staining is not suitable for the observation of some living cells because of its cytotoxicity or phototoxicity, and exogenous fluorescent protein labeling requires complex molecular biological processes[2-4].

On the contrary, when light passes through the transparent samples, the phase of optical wave changes and carries the information of samples due to the difference of refractive index between samples and surrounding media. Although phase component cannot be directly measured by optical detector, it is able to convert the changes of phase into changes of intensity, for example, Zernike phase contrast (PC) microscopy[5, 6] and differential interference contrast (DIC) microscopy[7] are two widely-used methods in cell phase imaging. Both techniques convert the phase difference of the sample into amplitude difference based on interference principle of light, thus the high contrast observation of unstained transparent samples can be realized. However, these two methods can only

 doi:10.20944/preprints202204.0109.v1

qualitatively characterize the phase information, but cannot quantify phase characteristics of the sample.

With the development of computational imaging, the phase information can be quantitatively retrieved through quantitative phase imaging (QPI) implementations including digital holography microscopy (DHM)[8-10], transport of intensity equations (TIE)[11-16], Fourier ptychography microscopy (FPM)[17-21], and quantitative differential phase contrast (qDPC) [22-24]. Compared with other imaging techniques, QPI can quantitatively measure the phase of biological samples with superiority of non-invasive, undamaged and high-definition, so it has become an important optical measurement technology in microscopy. In recent years, QPI techniques based on different principles have been proposed and successfully applied to the study of cell morphology, structure and dynamics[25-29].

Under the assumption of incoherent illumination, the qDPC microscopy and its variations single-shot qDPC present more convenient implementation condition than DHM, TIE and FPM methods and gains more attentions for high-speed QPI system. The new idea of qDPC is proposed by Phillips et al[30], in which the color-coded multiplexing strategy and multi-band filters are applied to achieve single-shot color-coded qDPC imaging (cDPC). Many researchers optimize the model for different imaging system components[31, 32] and illumination[33-37] to obtain better imaging quality. However, although the required image is reduced from four to one, the single-shot frame rate of qDPC is still much lower than that of the camera; and the existing devices are modified based on large-scale commercial and scientific microscopes, which are bulky, of high-cost, and not suitable for rural diagnosis, mobile treatment and other scenes.

To further increase the time-resolution of qDPC and provide mobile solutions, we designed a compact, real-time QPI system which can realize multimode imaging. The programmable LED array was used as illumination source directly, and the phase reconstruction algorithm was deployed on the graphics processing unit (GPU) of the laptop for calculation accelerating to achieve multimode real-time imaging including QPI. Our system can achieve high-contrast bright-field imaging, dark-field imaging and qDPC imaging of unstained phase samples at high frame rate. It also allows observation and tracking of fast-moving targets. Our system has a compact and stable structure, which is convenient to carry, and is suitable for special environments working conditions such as mobile biomedical treatment.

## 2. Materials and Methods

### *2.1. Principle of multimode imaging*

The various imaging modes are related to the illumination system, for example, the bright field (BF) is the full field of view (FOV) of transmitted light, the oblique illumination (OI) is off-axis, small angle illumination, and the dark field (DF) is large angle scattered light. According to the encodable circular LED array illumination as shown in figure 1, we can calculate the illumination numerical aperture (NA) of each layer of circular LED

$$NA_{illu} = \frac{R}{\sqrt{R^2 + D^2}}, \tag{1}$$

Where $R$ is the radius of the LED and $D$ is the distance between the source and the sample plane. Notice that the value of $NA_{illu}$ can be larger than NA of condenser under this direct illumination. While under Köhler illumination, $\alpha = \theta$, so $NA_{illu} = NA_{obj}$.

Preprints (www.preprints.org) | NOT PEER-REVIEWED | Posted: 12 April 2022 doi:10.20944/preprints202204.0109.v1

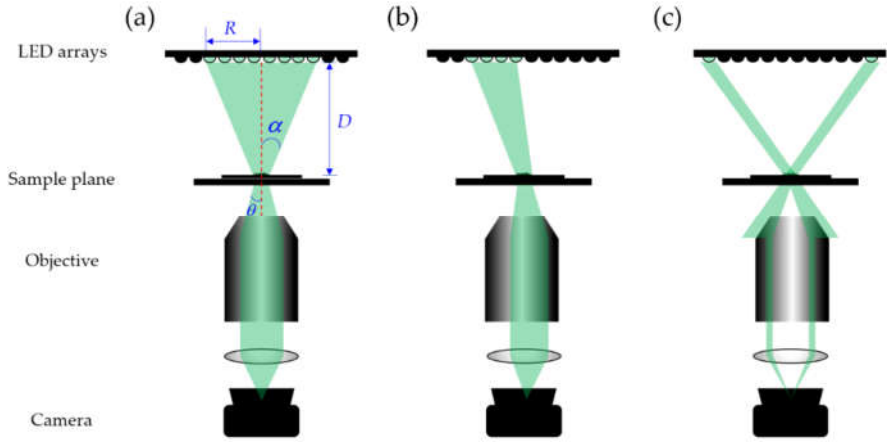


**Figure 1.** Diagram of circular LED array illumination and three traditional modes. (a) BF imaging. (b) OI imaging. (c) DF imaging.

BF is the most common imaging method in microscopy[38]. In this mode, $NA_{illu}$ is matched with $NA_{obj}$, as shown in figure 1 (a), the light source pass through the sample completely and enter the objective. In the BF image, the sample is dark, the brightness of FOV is high and uniform. OI imaging[39] uses partially illuminated light. When the light is obliquely incident through the sample as seen in figure 1 (b), the morphological difference of the sample surface modulates the light to form a phase difference, resulting in the optical path difference[4]. When the modulated light enters the objective, the image is half shaded and half bright and has a certain relief effect. DF is formed by annular illumination with a larger angle than OI, which meet the need of $NA_{illu} > NA_{obj}$. The sample is illuminated with light that cannot be collected by the objective (figure 1 (c)). Usually the background of FOV is dark, and the scattered light enters the objective to form a weak spot, which reflects the high-frequency information of the sample. This kind of imaging can clearly illustrate the edge contour of the sample[40].

After simple differential calculation and normalization[41], the DPC image with remarkable relief effect can be obtained by using two complementary and asymmetrical OI images in a certain direction, which are calculated by simple difference and normalized. For the QPI based on qDPC, we use color-coded multiplexing to achieve quantitative phase reconstruction of single-shot DPC and high efficiency real-time imaging. Referring to the existing research and report, qDPC using annular illumination can achieve better imaging contrast[1, 36, 37, 42]. As a result, the quantitative phase reconstruction is obtained under the three-equal annular illumination in our system. The specific process is as follows[24, 34]:

1. The unsampled pure color background corresponding to the tricolor channel is photographed respectively, and nine color response coefficients can be obtained after channel separation.
2. The LED array is encoded for illumination, and the images of corresponding color channel $I_R^{CCD}$, $I_G^{CCD}$, $I_B^{CCD}$ can be obtained by the camera.
3. A matrix composed of the nine color response coefficients acquired above is used to correct the color crosstalk of the captured image, so as to obtain the three-channel image needed for reconstruction

$$\begin{pmatrix} I_R \\ I_G \\ I_B \end{pmatrix} = \begin{pmatrix} F_{RR} & F_{RG} & F_{RB} \\ F_{GR} & F_{GG} & F_{GB} \\ F_{BR} & F_{BG} & F_{BB} \end{pmatrix} \begin{pmatrix} I_R^{CCD} \\ I_G^{CCD} \\ I_B^{CCD} \end{pmatrix}. \quad (2)$$

Preprints (www.preprints.org) | NOT PEER-REVIEWED | Posted: 12 April 2022 doi:10.20944/preprints202204.0109.v1

Where $F_{MN}$ is the corresponding $N$ color background image under $M$ channel ($M, N = R, G, B$). $I_X^{CCD}$ is the X channel image captured by the camera, and $I_X^{CCD}$ is the color image needed for computational reconstruction ($X = R, G, B$).

4. According to the differential analysis of different colors, the corresponding DPC image is calculated

$$I_R^{DPC} = \frac{(I_R - I_G) + (I_R - I_B)}{I_R + I_G + I_B},$$
$$I_G^{DPC} = \frac{(I_G - I_R) + (I_G - I_B)}{I_R + I_G + I_B}, \quad (3)$$
$$I_B^{DPC} = \frac{(I_B - I_R) + (I_B - I_G)}{I_R + I_G + I_B}.$$

5. After normalization of tricolor using the wavelength of green light, the phase transfer function (PTF) models are obtained by WOTF norm and subsequent related derivation[43-45]. Thus, the relationship between the DPC image and quantitative phase of the sample is established, and the phase is converted into intensity information. The QPI result can be obtained with constraint of Tikhonov regularization through the one-step deconvolution of DPC image and PTF

$$phase = \mathcal{F}^{-1}\left\{\frac{\sum_i \left[PTF_i^* \cdot \mathcal{F}\left(I_i^{DPC}\right)\right]}{\sum_i \left(\left|PTF_i\right|^2\right) + \alpha}\right\}. \quad (4)$$

Where $\mathcal{F}$ is Fourier transform, $\mathcal{F}^{-1}$ is inverse Fourier transform, * denotes conjugation, $i$ is the color channel of DPC, $\alpha$ is the regularization parameter. The value of $\alpha$ is determined by the characteristics of the imaging system, if the value is too large, the phase distribution will be compressed; if the value is too small, it will amplify the systematic noise and affect the quality of phase reconstruction.

### *2.2. Overall design of the setup*

Programmable annular LED array is used as the source in our self-designed microscopic imaging system, and control signals from the personal computer (PC) is sent to the micro control unit (MCU) (Arduino UNO, USA) to control the 61-bit programmable LED array to provide multimode illumination. The light is converted into parallel light by the infinity objective, then passes through a tube lens with focal length of 175mm, and is reflected twice by silver-plated mirrors M1 and M2. Finally, it is condensed on the camera (MV-SUA230GC-T, Mindvision, China) for imaging and the outputs are sent back to PC, as shown in figure 2 (a). With modular design, our system can be divided into four parts, including programmable LED illumination module, two-dimensional (2D) electronic control module, axial high-precision focus module, and eccentric imaging module (figure 2 (b)).

The programmable the LED illumination module contains a 61-bit programmable annular LED multi-layer array as the light source with plug-in design. It is convenient for users to change and calibrate the illumination patterns accounting for actual needs. The three-dimensional (3D) displacement between LED and rack can be adjusted at the range of ±5mm. It also has locking function which is easy for secondary calibration of the optical axis.

The electronic control platform module is designed as a three-layer structure. The bottom layer connects the system shell to determine the direction. The medium layer is X-axis control platform. As a connector, it can drive the Y-axis control platform (the top layer) so as to reduce the friction between the two axes. The core components are roller guide and screw motor. The roller guide serves as the connection between the upper and

Preprints (www.preprints.org) | NOT PEER-REVIEWED | Posted: 12 April 2022 doi:10.20944/preprints202204.0109.v1

lower layers, and play the role of fixed direction combined with the slot. The screw motor provides transmission so that the platform can complete automatic 2D control.

The axial high-precision focus module uses one-dimensional high-precision displacement control platform combined with an eccentric objective bracket. The center of objective is matched with that of tube lens. Objective focusing will be realized via this module.

The eccentric imaging module allows the light converges along the edge of shell to the camera through two times of reflection, which makes the optical path compact and greatly reduces the overall volume of the system. With the volume of 140 × 165 × 250mm$^3$, our setup is portable to work at different scenes.

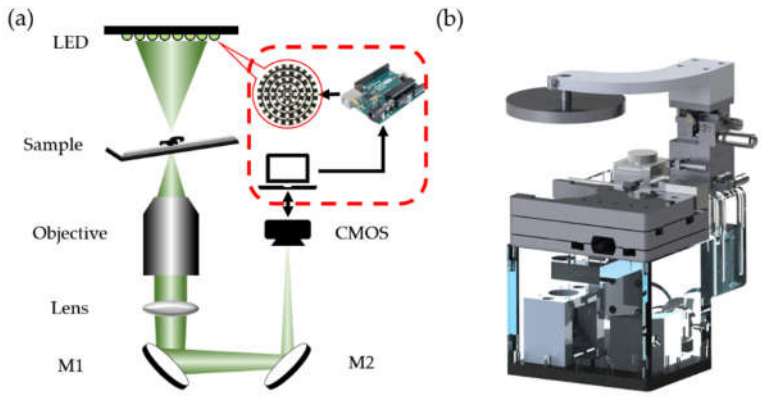


**Figure 2.** Diagram of imaging and physical design of the system. (a) Schematic of imaging. (b) Physical design.

*2.3. Hardware control of system*

Hardware control is divided into camera control and MCU control. Camera control is to set the corresponding parameters of the camera, combined with related algorithms to achieve high-quality imaging. MCU control is about the control of LED illumination, and motor platform movement. Serial communication is established between Arduino and PC, which can be divided into three types of control, including control of LED to realize multimode illumination, control of screw motor and displacement platform to realize 3D automatic control, and control of tricolor to realize brightness adjustment of LED.

The setup can encode the LED array to present corresponding illumination pattern and imaging mode according to observation requirements, control the lateral position through the stepper motor, and use the high-precision Z-axis displacement platform to realize axial focusing. The region of interest (ROI) of the camera can be set through PC Then the best image contrast is obtained by adjustment of camera parameters., and the CMOS camera is used to achieve real-time sampling.

The MCU used in this system is Arduino UNO. This is a convenient, flexible, easy-to-use and open-source platform, with 14 I/O pins, external 5 voltage power supply and ground wire. The integrated development environment (IDE) of Arduino is based on Java open-source programming platform, using internal function library.

The light source is WS2812B intelligent external control integrated LED. Its characteristic parameters are shown in table 1. Combined with 256 levels, 256$^3$ kinds of color lighting patterns can be realized.

The 20H33 screw motor (2mm lead) is applied as the drive of the horizontal 2D displacement platform. The vibration caused by the rotational motion and the offset caused by mistakenly touching, can be reduced by the stepper motor. XM50H-25-PU small-stroke displacement platform is adopted in the axial direction, in which the resolution of the stepper can reach 2.5um, and the steel platform structure also ensures a certain axial load-bearing capacity.

**Table 1.** Characteristic parameters of WS2812B LED.

Preprints (www.preprints.org) | NOT PEER-REVIEWED | Posted: 12 April 2022 doi:10.20944/preprints202204.0109.v1

| Color | Wavelength / nm | Illuminance / mcd | Rated Current / mA | Rated Voltage / V |
|---|---|---|---|---|
| Red | 620~630 | 550~700 | 20 | 1.8~2.2 |
| Green | 515~530 | 1100~1400 | 20 | 3.0~3.2 |
| Blue | 465~475 | 200~400 | 20 | 3.2~3.4 |

*2.4. Algorithm development and deployment*

In order to achieve real-time QPI, we rewrite the cDPC algorithm based on GPU parallel computing acceleration, called GPU-cDPC, as shown in figure 3. First, the data-independent parameter initialization and preprocessing deployment are completed on GPU, including the pre-obtained color response matrix, spatial sampling, settings of pupil and illumination, and the PTF model calculated based on WOTF. Then the MCU is used to control the LED array to show annular illumination patterns. When the image is captured by the camera, the three-color channel is separated to obtain $I_R^{CCD}$, $I_G^{CCD}$, $I_B^{CCD}$. After calibration of color crosstalk using equation (2), the images are transmitted to GPU, then the DPC images are calculated by equation (3), resulting in tricolor DPC images $I_R^{DPC}$, $I_G^{DPC}$, $I_B^{DPC}$.

Next, the tricolor DPC images are processed by 2D fast Fourier transform (2D-FFT), and multiplied by the calculated PTF model with the constraint of Tikhonov regularization. The FD expression of the reconstructed phase is obtained. Finally, the QPI result (corresponding to equation (4)) can be obtained after a 2D inverse fast Fourier transform (2D-IFFT). And the phase image is retransmitted from GPU to central processing unit (CPU) for preservation and other operations.

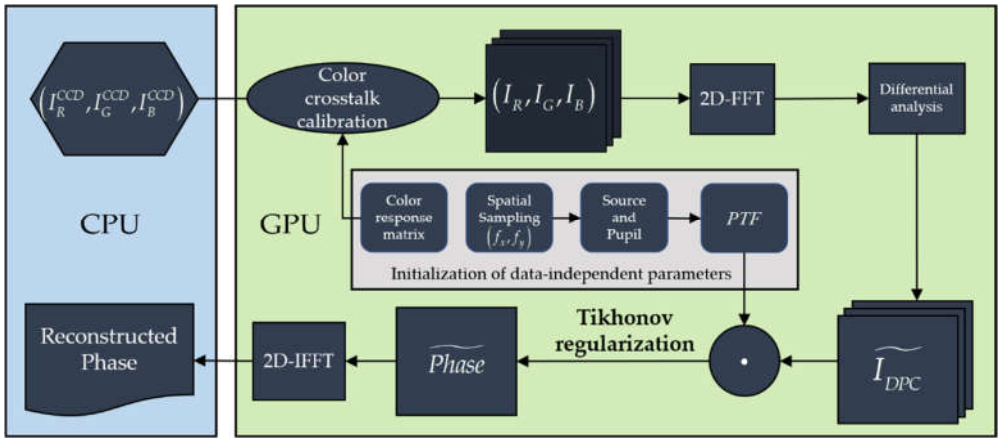


**Figure 3.** GPU-qDPC block diagram. The interior of the middle gray block diagram represents the data-independent parameters that need to be deployed on the GPU in advance.

*2.5. Sample preparation*

Hela cells were suspended in 2 mL culture medium containing 10% FBS and seeded into a 60-mm culture dish (Biosharp, China, 5.2 × $10^6$ cells per dish). After the generation of cells adhere to the wall, we use the self-developed microscope and CMOS camera to obtain multimode imaging of the samples. It is similar to the preparation of NIH-3T3 cells.

The semen was treated by direct swim-up (DSU) method. First, 3 ml of prewarmed sperm wash medium (SpermRinse, Vitrolife, Sweden) was added into the centrifuge tube. Second, 3 ml of raw semen was added with a straw to form a liquid layer under the washing medium. Third, the centrifuge tube was inclined at an angle of 45° and incubated for 30 min in a 6% CO2 incubator at 37°C. Forth, the test tube was put upright, and about 1.5 ml of the upper medium layer was suck and transferred into a centrifuge tube and following by centrifugation for 15 min at 1250 rpm. The supernatant was discarded after centrifuge. Finally, the semen was resuspended by adding an appropriate amount of

Preprints (www.preprints.org) | NOT PEER-REVIEWED | Posted: 12 April 2022 doi:10.20944/preprints202204.0109.v1

fertilization medium (Cook, Sydney, Australia). The study protocol was reviewed and approved by Biomedical Ethics Committee of Anhui Medical University (20210744).

## 3. Results

### *3.1. Accuracy of phase reconstruction*

Before measuring the phase for biomedical samples, we first evaluate the accuracy of phase retrieval of our self-developed system. The focal star of 200nm thickness in Quantitative phase target (QPT, Benchmark, USA) is imaged by an objective (10×, NA=0.3). After the image is captured, it is transmitted to a laptop for GPU-cDPC algorithm calculation. According to the single RGB image as shown in figure 4 (a1), the phase image of focal star (a2) is obtained. Generally, a clear phase image of the sample can be obtained, but there is a certain ghosting in the image, and the gray distribution is not uniform.

Figure 4 (a3) shows the phase reconstruction accuracy of our setup by measurement of gray value distribution along the red line in (a2). The refractive index of QPT is 1.52, the thickness is 200nm, so the phase of ground truth is (-1.8261, 1.8261). The focal star consists of 40 fans, and the angular length of each piece is $\pi/40$ rad. Herein, the phase distribution of ground truth can be drawn in the blue line square wave in (a3). The red line denotes the reconstruction of our setup. The results illustrate that the first half of red line in (a2), that is, the green dotted box in (a3), is more accurate, and the average error of the phase is 9.7%. But other parts are much larger, with a maximum of 40.3%. In (a3), the width of red wave crest is basically consistent with blue square wave, indicating high measurement accuracy of angular length of QPT, and the error is close to 1.4%.

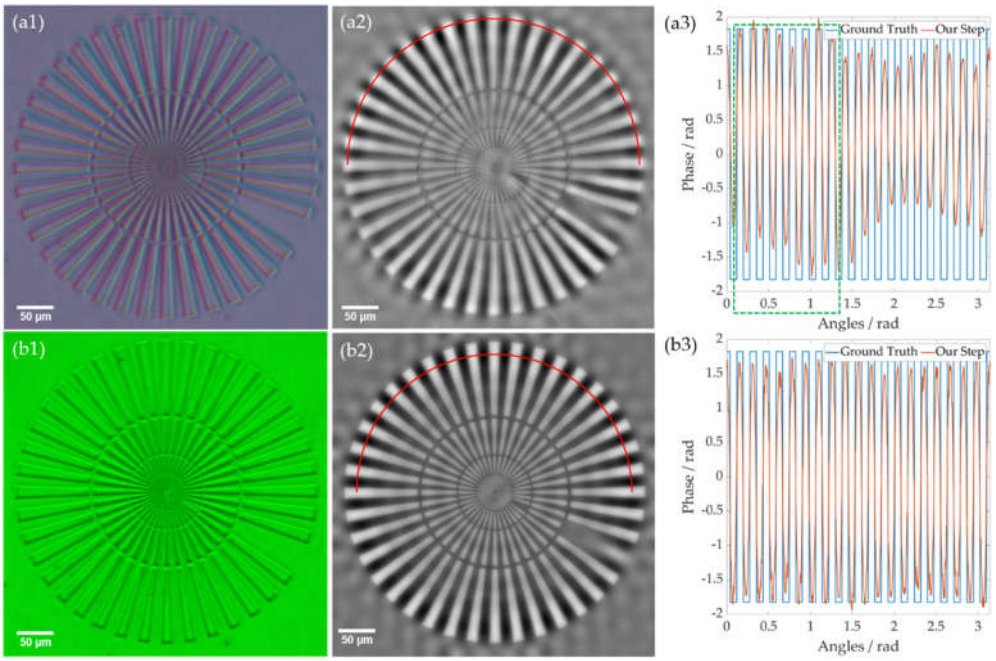


**Figure 4.** Phase image and quantitative measurement results of QPT. (a) Results of cDPC algorithm. (b) Results of tDPC algorithm. (a1) and (b1) are initial images of 200nm focal star captured by CMOS, and (b1) is one of the four OI images. (a2) and (b2) are the corresponding phase images. (a3) and (b3) are the phase distribution along the red line starting from the left side in (a2), (b2). The abscissa is the angle, the ordinate is the phase value, the blue represents the phase distribution of ground truth, the red is reconstruction result.

In addition to using the idea of color-coded multiplexing to achieve single-shot cDPC phase reconstruction, our system can also use traditional two orthogonal axes DPC images (tDPC) to complete phase reconstruction. The experimental condition is the same as cDPC.

Preprints (www.preprints.org) | NOT PEER-REVIEWED | Posted: 12 April 2022 doi:10.20944/preprints202204.0109.v1

Compared with (a2), it is obvious that the result (b2) of tDPC imaging using monochromatic light has better contrast and resolution. Further comparing (a3) and (b3), tDPC also has a better performance in terms of measurement accuracy and stability with error of 4.9%, while the angular length accuracy of the two measurements is the same basically, which is in good agreement with ground truth.

### *3.2. Real-time QPI of swimming sperms*

We then use this device to perform real-time QPI of unlabeled sperm with high motility, using the same regularization constraints ($\alpha$=0.005) as phase measurement. The frame rate of camera is 20 fps, FOV is 950 × 600 pixels, and objective is 20×, NA=0.5. The control of software and hardware, image acquisition and processing are carried out on laptop (AMD R7 5800H, RTX3070, 32GB RAM). The 1.5μl sperm solution is diluted 100 times by adding 7% Polyvinylpyrrolidone (PVP), and the imaging experiment started half an hour later (see video 1).

The time sequence images of the two motile sperms in the video is analyzed respectively, as shown in figure 5. At the beginning, the sperm A is out of focus, and it moves along the lower left with a certain axial upward movement (our device is an inverted structure), coming to the focal plane presented in (a2). (a3) shows the image of sperm A at the maximum defocus displacement at 0.9s. At around 1.65s, the sperm moves downward and approaches the focal plane in (a4). While the sperm B has no obvious axial movement and swims along the vertical direction. We only track the movement of sperm B from video 1 because of the defocus of sperm A, as shown in the green line of figure 5. The curvilinear velocity (VCL) of sperm B is calculated of 41.4μm/s from tracking. It is similar to the average VCL of 42.8μm/s from clinical examination following the standard of WHO[46], verifying the good real-time performance of our system.

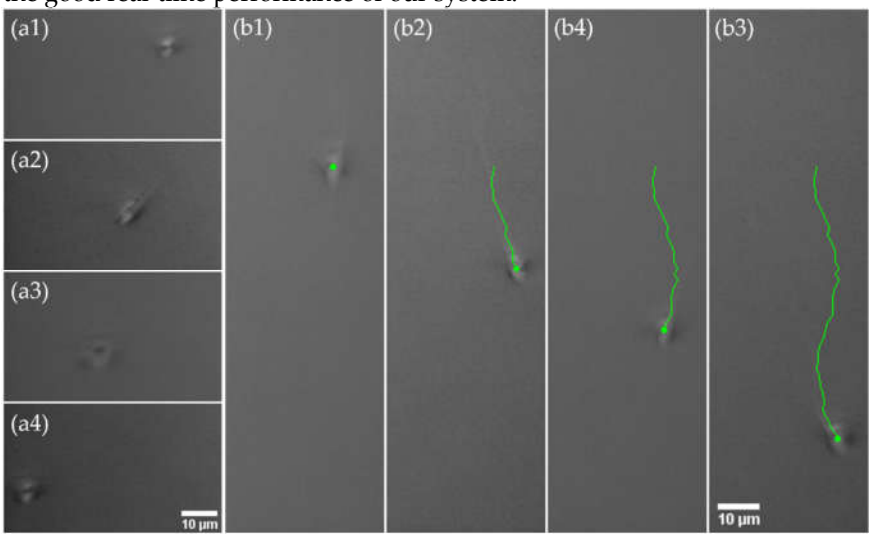


**Figure 5.** Time sequence analysis of motile sperms. (a) Sperm A on the left in video 1. (b) Sperm B on the right in video 1. (a1-a4) and (b1-b4) are the phase images of two sperms at 0, 0.5, 0.9, and 1.65 seconds, respectively. The green line is the trajectory of sperm B.

### *3.3. Multimode imaging of different cell samples*

We use the system to carry out two QPI methods of different unlabeled samples, and the relevant parameters are consistent with the phase measurement above. Figure 6 shows the results of multimode imaging of Hela cells. (a) shows a full FOV cDPC imaging of Hela cells. From the magnified images in yellow box, the corresponding BF, DF, cDPC, tDPC results can be obtained. For the sample has weak absorption, it is difficult to see the cells except thick areas in the BF (b). Because of the light scattering of thick areas and edges of the cell, the outline can be seen in the DF (c), but the details cannot be seen clearly.

Preprints (www.preprints.org) | NOT PEER-REVIEWED | Posted: 12 April 2022 doi:10.20944/preprints202204.0109.v1

Based on PTF model, the relationship between the phase and amplitude (intensity) of the sample is established. Consequently, QPI can improve the imaging contrast and see more tiny structures of cells, as shown in (d) and (e). While displaying the phase information of the sample, QPI can improve the imaging contrast and demonstrate more tiny structures of cells. The white arrows in the cDPC image (d) point to the nucleolus of Hela cells, while the same ROI of (e) has better contrast and resolution. Compared with (d), the tDPC image can present more information, as seen in the white dotted circles in (e).

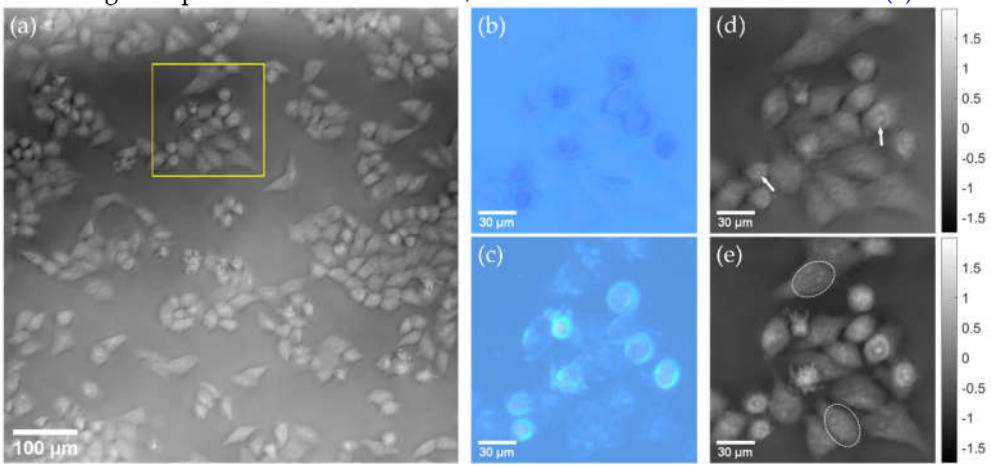


**Figure 6.** Multimode imaging of human cervical cancer cells (Hela cells). (a) cDPC imaging with FOV of 1200 × 1200 pixels. (b)-(e) are the BF, DF, cDPC, tDPC images corresponding to the yellow box in (a), respectively.

We also carry out the multimode imaging towards mouse embryonic fibroblasts (NIH-3T3 cells), as presented in figure 7. Similarly, the nucleolus of NIH-3T3 can be observed by cDPC as pointed with the white arrow in (d) compared to BF and DF imaging, while tDPC can further improve the contrast and resolution than cDPC, presenting the detail structure which cannot be distinguished by cDPC image can be observed, as seen in white dotted circle from (e).

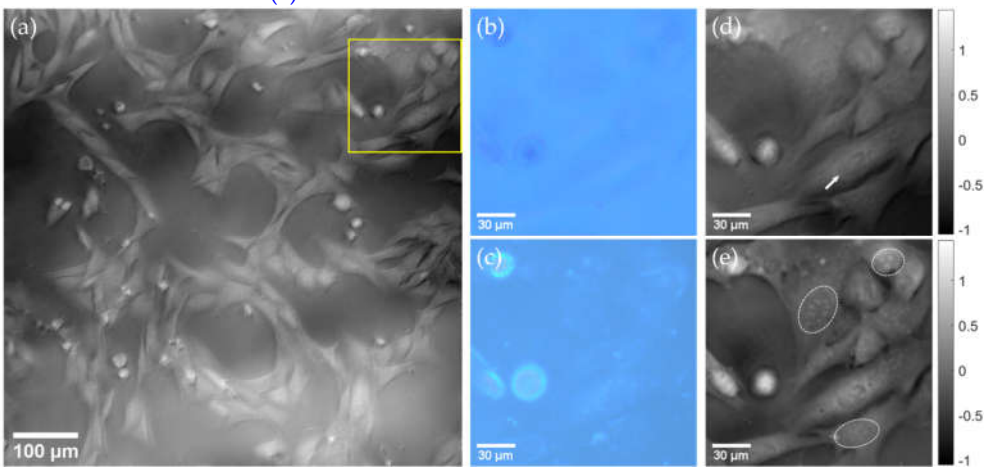


**Figure 7.** Multimode imaging of mouse embryonic fibroblasts (NIH-3T3 cells). (a) cDPC imaging with FOV of 1200 × 1200 pixels. (b)-(e) are the BF, DF, cDPC, tDPC images corresponding to the yellow box in (a), respectively.

Compared with the existing single-shot cDPC results[34], although the accuracy of phase reconstruction is relatively close, there is still a certain gap of the imaging quality between ours and the improved commercial microscopy as our system does not have any lens group to reduce chromatic aberration and other aberrations. In figure 6 and figure 7,

 doi:10.20944/preprints202204.0109.v1

the phase distribution of the two methods is identical generally, but the phase image of tDPC has no ghosting, and has better contrast and resolution. It is noteworthy that although the contrast of tDPC image is more uniform than that of cDPC, it cannot completely remove the "cloud" effect (as shown in (a2), (b2) of figure 4, and (d), (e) of figure 6, figure 7) to achieve the ideal uniform imaging effect.

## 4. Discussion

### *4.1. Comparison of phase reconstruction results between cDPC and tDPC*

The differences between cDPC and tDPC images are caused by different principles. Although the PTF models of the two methods are similar, cDPC uses three different wavelengths of light to make phase construction. Different wavelengths will cause the focal plane to be distributed in different axial positions, which called chromatic aberration. Chromatic aberration will lead to defocus on a focal plane, so the amplitude noise is introduced into the PTF model of the ideal DPC, and the amplitude term is zero no longer. This affects the resolution of the reconstructed phase image, and the image information has phase-amplitude coupling. Although the phase reconstruction accuracy of our device is similar to that reported in [34], the setup has not added lens groups or components to eliminate chromatic aberrations yet, and 3D printing materials are used to complete the assembly of system. Its own printing error may cause the offset of optical axis, resulting in ghosting. There is still a certain gap between the reconstructed phase image contrast and resolution and the existing improved commercial microscopic devices based on DPC principle, but the tDPC results are comparable.

Moreover, the PTF model assumes that the light source is a parallel surface light source and the sample is a weak object, the influence of light on its amplitude and phase is relatively small, so the amplitude and phase of the complex transmission field can be linearly represented by the weak object approximation (WOA), thus the sample phase and amplitude can be separated. However, due to the influence of such factors as chromatic aberration, illumination distance and LED illuminance, the light from each LED may not be a plane wave, resulting in an uneven intensity distribution of FOV. For tissue or cell sample, its own light scattering and absorption is not far less than the incident light (the edge image in the DF is clear), and does not meet the WOA condition. The reconstructed phase may not correspond to the ground truth.

The Tikhonov regularization norm is added to reduce the adverse influence of background and impurities noise on the overall imaging resolution and contrast. However, if the value is too small, there will be artifacts at the edge of the cell, and the noise will be magnified, which will make the phase image more uneven, resulting in a "cloud" effect; if the value is too large, the calculated phase will be compressed, which can not correspond to the ground truth of sample. Can we find a new constraint method to further optimize the existing PTF deconvolution results? This may be a spotlight worth exploring in the field of qDPC.

### *4.2. Comparison of real-time imaging based on CPU and GPU*

We compare the effects of different computing devices on real-time performance. The laptop (AMD R7 5800H, RTX3070, 32GB RAM) is used to compare the time cost of cDPC algorithm deployed on CPU by default and that accelerated by GPU. As shown in table 2, the frame rate of cDPC deployed on CPU is only 7.5 fps, while that of imaging based on GPU acceleration is stable at more than 60 fps, which is nearly 10 times faster than the CPU! Therefore, our system using GPU-cDPC can be used for real-time phase imaging of samples with high mobility (such as the above swimming sperms).

We compare the real-time QPI performance deployed on CPU and GPU in sample observation, as presented in video 2-1 and video 2-2. The FOV is 1200 × 1200 pixels, objective is 20×, NA=0.5, and the sample is mouse testicular tissue section. The frame rate of GPU acceleration is significantly higher than that of CPU, and the results on CPU will lose

 doi:10.20944/preprints202204.0109.v1

sample information during motor stepping due to low frame rate. However, limited to camera frame rate (20 fps), performance of GPU acceleration has not been fully released.

**Table 2.** Time cost of cDPC algorithm based on CPU and GPU.

| Devices | Time cost per frame / ms | Frames per second |
|---|---|---|
| AMD R7 5800H | 133.4 ± 2.51 | 7.5 |
| NVIDIA RTX3070 (GPU) | 14.6 ± 0.46 | 68.5 |

## 5. Conclusions

In this paper, we propose a compact real-time QPI system. The imaging principle and device design are described, and the performance of phase reconstruction accuracy, imaging contrast, resolution and real-time QPI are tested in QPT and different biological samples. Generally, the device has the following characteristics:

The microscope has the advantages of compact structure, small size, stable structure, easy to carry and can work in special scenes such as mobile medical treatment. Axial focusing and sample observation can be realized without manual intervention by the electronic control of 3D displacement. The setup can be equipped with a high-performance laptop for real-time QPI, improving imaging contrast and reflecting more quantitative details of the sample.

Compared with the existing improved commercial microscopic devices, our self-designed devices sacrifice a certain imaging contrast for more high-speed and portable real-time imaging. At present, the whole device is assembled by 3D printing materials, and the components and lens groups with functions such as eliminating aberrations have not yet been added. After metalworking, we will supplement the corresponding components. We firmly believe that in the future it will have a better performance in portable multimode imaging applications.

**Supplementary Materials:** The following supplementary materials will be uploaded with this manuscript, including video 1, video 2-1, and video 2-2.

**Author Contributions:** Conceptualization, Tao Peng, Rongsheng Lu and Jinhua Zhou; methodology, Tao Peng, Zeyu Ke and Shuhe Zhang; software, Tao Peng and Zeyu Ke; validation, Shuhe Zhang and Meng Shao; formal analysis, Tao Peng and Meng Shao; investigation, Tao Peng, Zeyu Ke, Xiao Liu and Han Yang; resources, Huijuan Zou, Hui Shi, Zhensheng Zhong, Shu fang, Jinhua Zhou; writing—original draft preparation, Tao Peng, Zeyu Ke, Han Yang and Mincheng Zhong; supervision, Rongsheng Lu and Jinhua Zhou. All authors have read and agreed to the published version of the manuscript.

**Funding:** This research was funded by Jinhua Zhou of Natural Science Foundation of Anhui Province in China, grant number 1908085MA14, and Research Fund of Anhui Institute of Translational Medicine, grant number 2021zhyx-B16; Hui Shi of Natural Science Foundation in China, grant number 12004008; Shu Fang of Natural Science Foundation of Anhui Provincial Education Department, grant number KJ2021A0251.

**Data Availability Statement:** Not applicable.

**Acknowledgments:** Thanks for the donation of materials used for experiments from Prof. Fengsong Wang, College of Life Sciences, Anhui Medical University.

**Conflicts of Interest:** The authors declare no conflict of interest.

## References

[1] Yao Fan, Qian Chen, Jiasong Sun, Zuxin Zhang, Linfan Lu, C. Zuo. Review of the development of differential phase contrast microscopy. Infrared and Laser Engineering, 2019, 48, 224-243.

[2] N. Lue, W. Choi, G. Popescu, T. Ikeda, M.S. Feld. Quantitative phase imaging of live cells using fast Fourier phase microscopy. Appl Optics, 2007, 46, 1836-1842.

[3] Masters, R. Barry. Quantitative Phase Imaging of Cells and Tissues. J Biomed Opt, 2012, 17, 029901.

[4] X. Xiong, Research On Quantitative Differential Phase Contrast Imaging In An LED Array Microscope. Master, University of Electronic Science and Technology of China, Xian, Shanxi Province, China, June, 2018.

[5] C.R. Burch, J.P.P. Stock. Phase-Contrast Microscopy. Journal of Scientific Instruments, 1942, 19, 71-75.

[6] F. Zernike. How I Discovered Phase Contrast. Science, 1955, 121, 345-349.

[7] M.R. Arnison, K.G. Larkin, C. Sheppard, N.I. Smith, C.J. Cogswell. Linear phase imaging using differential interference contrast microscopy. J Microsc, 2010, 214, 7-12.

[8] E. Cuche, F. Bevilacqua, C. Depeursinge. Digital holography for quantitative phase-contrast imaging. Opt Lett, 1999, 24, 291-293.

[9] I. Yamaguchi. Phase-shifting digital holography. Opt Lett, 2000, 22, 1268-1270.

[10] U. Schnars, W. Jüptner. Digital holography and numerical reconstruction of holograms (REVIEW ARTICLE). Meas Sci Technol, 2002, 13, 85.

[11] T.E. Gureyev, A. Roberts, K.A. Nugent. Partially coherent fields, the transport-of-intensity equation, and phase uniqueness. J Opt Soc Am A, 1995, 12, 1942-1946.

[12] C. Zuo, Q. Chen, W. Qu, A. Asundi. High-speed transport-of-intensity phase microscopy with an electrically tunable lens. Opt Express, 2013, 21, 24060-24075.

[13] C. Zuo, Q. Chen, Y. Yu, A. Asundi. Transport-of-intensity phase imaging using Savitzky-Golay differentiation filter - theory and applications. Opt Express, 2013, 21, 5346-5362.

[14] C. Zuo, Q. Chen, A. Asundi. Boundary-artifact-free phase retrieval with the transport of intensity equation: fast solution with use of discrete cosine transform. Opt Express, 2014, 22, 9220-9244.

[15] L. Huang, C. Zuo, M. Idir, W. Qu, A. Asundi. Phase retrieval with the transport-of-intensity equation in an arbitrarily shaped aperture by iterative discrete cosine transforms. Opt Lett, 2015, 40, 1976-1979.

[16] J. Zhang, Q. Chen, J. Sun, L. Tian, C. Zuo. On a universal solution to the transport-of-intensity equation. Opt Lett, 2020, 45, 3649-3652.

[17] G. Zheng, R. Horstmeyer, C. Yang. Wide-field, high-resolution Fourier ptychographic microscopy. Nat Photonics, 2013, 7, 739-745.

[18] X. Ou, G. Zheng, C. Yang. Embedded pupil function recovery for Fourier ptychographic microscopy. Opt Express, 2014, 22, 4960-4972.

[19] L. Tian, Z. Liu, L.-H. Yeh, M. Chen, J. Zhong, L. Waller. Computational illumination for high-speed in vitro Fourier ptychographic microscopy. Optica, 2015, 2, 904-911.

[20] J. Sun, Q. Chen, J. Zhang, Y. Fan, C. Zuo. Single-shot quantitative phase microscopy based on color-multiplexed Fourier ptychography. Opt Lett, 2018, 43, 3365-3368.

[21] S. Song, J. Kim, S. Hur, J. Song, C. Joo. Large-Area, High-Resolution Birefringence Imaging with Polarization-Sensitive Fourier Ptychographic Microscopy. ACS Photonics, 2021, 8, 158-165.

[22] D.K. Hamilton, C.J.R. Sheppard. Differential phase contrast in scanning optical microscopy. J Microsc, 1984, 133, 27-39.

[23] S.B. Mehta, C.J.R. Sheppard. Quantitative phase-gradient imaging at high resolution with asymmetric illumination-based differential phase contrast. Opt Lett, 2009, 34, 1924-1926.

[24] L. Tian, L. Waller. Quantitative differential phase contrast imaging in an LED array microscope. Opt Express, 2015, 23, 11394-11403.

[25] H. Pham, H. Ding, N. Sobh, M. Do, S. Patel, G. Popescu. Off-axis quantitative phase imaging processing using CUDA: toward real-time applications. Biomed Opt Express, 2011, 2, 1781-1793.

[26] G. Popescu. Quantitative phase imaging in biomedicine. Conference on Lasers and Electro-Optics 2012, San Jose, California, USA, 6th May, 2012.

[27] B. Kemper, P. Langehanenberg, S. Kosmeier, F. Schlichthaber, C. Remmersmann, G. von Bally, C. Rommel, C. Dierker, J. Schnekenburger. In Digital Holographic Microscopy: Quantitative Phase Imaging and Applications in Live Cell Analysis, 1st ed.; V.V. Tuchin Eds.; Springer New York: New York, NY, 2013; pp.215-257.

[28] Y. Kim, H. Shim, K. Kim, H. Park, S. Jang, Y. Park. Profiling individual human red blood cells using common-path diffraction optical tomography. Sci Rep, 2014, 4, 6659.

[29] L. He, M. Shao, X. Yang, L. Si, M. Jiang, T. Wang, Z. Ke, T. Peng, S. Fang, S. Zhang, X. Ouyang, G. Zhao, J. Zhou. Morphology analysis of unlabeled red blood cells based on quantitative differential phase contrast microscopy, Cytom Part A, 2022, accepted.

[30] Z.F. Phillips, M. Chen, L. Waller. Single-shot quantitative phase microscopy with color-multiplexed differential phase contrast (cDPC). PLoS One, 2017, 12, e0171228.

[31] C. Zuo, Q. Chen, J. Sun, S. Feng, G. Gu, Y. Zhang, Y. Hu, T. Tao, J. Li, L. Zhang, Programmable aperture microscope system based on LCD liquid crystal panel and multi-mode imaging method thereof, in China, 2016.

[32] C. Zuo, J. Sun, S. Feng, M. Zhang, Q. Chen. Programmable aperture microscopy: A computational method for multi-modal phase contrast and light field imaging. Opt Laser Eng, 2016, 80, 24-31.

[33] D. Lee, S. Ryu, U. Kim, D. Jung, C. Joo. Color-coded LED microscopy for multi-contrast and quantitative phase-gradient imaging. Biomed Opt Express, 2015, 6, 4912-4922.

[34] W. Lee, D. Jung, S. Ryu, C. Joo. Single-exposure quantitative phase imaging in color-coded LED microscopy. Opt Express, 2017, 25, 8398-8411.

[35] W. Lee, J.H. Choi, S. Ryu, D. Jung, J. Song, J.S. Lee, C. Joo. Color-coded LED microscopy for quantitative phase imaging: Implementation and application to sperm motility analysis. Methods, 2018, 136, 66-74.

[36] Y. Fan, J. Sun, Q. Chen, X. Pan, L. Tian, C. Zuo. Optimal illumination scheme for isotropic quantitative differential phase contrast microscopy. Photonics Res, 2019, 7, 890-904.

[37] Y. Fan, J. Sun, Q. Chen, X. Pan, M. Trusiak, C. Zuo. Single-shot isotropic quantitative phase microscopy based on color-multiplexed differential phase contrast. APL Photonics, 2019, 4, 121301.

[38] L. Xue, Optical microscopy imaging and its application in bio-sample display and measurement. Ph.D, Nanjing University of Science and Technology, Nanjing, Jiangsu Province, China, May, 2013.

[39] P.J. Shaw, D.A. Agard, Y. Hiraoka, J.W. Sedat. Tilted view reconstruction in optical microscopy. Three-dimensional reconstruction of Drosophila melanogaster embryo nuclei. Biophys J, 1989, 55, 101-110.

[40] X. He, Research On Multi-mode Microscopic Imaging Technology Of Brightfield, Darkfield, Phase Contrast. Master, University of Electronic Science and Technology of China, Xian, Shanxi Province, China, June, 2017.

[41] Z. Liu, L. Tian, S. Liu, L. Waller. Real-time brightfield, darkfield, and phase contrast imaging in a light-emitting diode array microscope. J Biomed Opt, 2014, 19, 106002.

[42] Y. Fan, J. Sun, Q. Chen, J. Zhang, C. Zuo. Wide-field anti-aliased quantitative differential phase contrast microscopy. Opt Express, 2018, 26, 25129-25146.

[43] D.K. Hamilton, C.J.R. Sheppard, T. Wilson. Improved imaging of phase gradients in scanning optical microscopy. J Microsc, 1984, 135, 275-286.

[44] Streibl, N. Three-dimensional imaging by a microscope. J Opt Soc Am A, 1985, 2, 121-127.

[45] M.H. Jenkins, T.K. Gaylord. Quantitative phase microscopy via optimized inversion of the phase optical transfer function. Appl Optics, 2015, 54, 8566-8579.

 doi:10.20944/preprints202204.0109.v1

[46] D.T.G. Cooper, C.o.R.M.a.A.o.t. University, G. Münster. WHO laboratory manual for the Examination and processing of human semen, 5 th ed.; WHO Press: 20 Avenue Appia, 1211 Geneva 27, Switzerland, 2010; pp.117.